Reliability Modeling and Analysis of High-Power Medium-Voltage Power Electronic Transformers

Jun Jiang, *Senior Member, IEEE*, Beibei Chen, Qingwei Zhu, Xuefeng Duan, and Renli Fu

***Abstract*—High-power medium-voltage power electronic transformers (PETs) are core equipment to convert and control electrical power with high efficiency in hybrid ac/dc power grids. PET typically consists of functional semiconductor devices and high-frequency transformers (HFTs), and its reliability is vital to be assessed for the upcoming utilization. In this article, a reliability evaluation method for PETs based on one of the most prevalent topologies, i.e., MMC configuration, is proposed, where the operational conditions and the main components are accounted. First, the power losses and junction temperature distribution of insulated gate bipolar transistor modules used in the rectification, isolation, and inversion stages of the MMC-based PET are analyzed in detail. The device failure rate is then evaluated based on reliability assessment criteria. Second, considering that the insulation system is a particularly vulnerable point in the HFT unit, a PET system reliability model is constructed accounting for the series-parallel connection among components in the topology. Finally, the mean time to failure of the PET equipment with a 10 kW/20 kHz HFT prototype is estimated to be 1.42 years according to the proposed model, and the influence of switching frequency on PET reliability is further analyzed. The proposed PET reliability can provide as a theoretical reference for the optimized design and operational maintenance of promising high-power medium-voltage PET equipment in power grid.**

***Index Terms*—Failure rate, high frequency transformer, mean time to failure, power electronic transformer, reliability modeling.**

I. Introduction

HIGH-POWER medium-voltage power electronic transformers (PETs) are supposed to convert and control electrical power, leading to a compact design and efficient power conversion. Due to their flexible power flow control capability and high interface compatibility, PETs show broad application prospects in renewable energy grids, transportation, energy storage, and EV fast-charging deployments [1], [2], [3]. PETs contain numerous power electronic devices, such as insulated gate bipolar transistor (IGBT) modules. Their operating conditions are complex, and power losses are significant [4], [5]. Particularly, under high-power-density and high-switching-frequency conditions, the junction temperature of IGBT modules rises sharply, accelerating equipment aging and reducing PET reliability [6], [7], [8]. Meanwhile, high-frequency transformer (HFT) is another essential unit in a typical PET equipment, and it endures high-frequency, high-voltage, fast-rising pulse electrical stress and high thermal stress. The harsh environment accelerates insulation material degradation and increases breakdown risks, further compromising system reliability. Insufficient reliability has become a key bottleneck limiting the widespread application of high-power medium-voltage PET. Accurately assessing the operational reliability of these devices remains a critical challenge that must be urgently addressed to ensure the safety and stability of new-type power systems [9], [10].

According to the PET reliability research statistics, up to 34% of failures are attributed to malfunctions in power switching devices [11], underscoring their role as a primary factor affecting PET reliability. In existing studies, the reliability of power devices has been primarily examined in terms of voltage levels and operational characteristics across various application scenarios. In the field of renewable energy, such as wind turbine converter systems, reliability is significantly influenced by environmental factors. It has been demonstrated that junction temperature swings in IGBT modules of doubly-fed induction generator converters are drastically induced by wind speed fluctuations. It is necessary to incorporate dynamic thermal stress into fatigue accumulation calculation through failure mechanism modeling [12]. Furthermore, multitime-scale operational reliability evaluation methods have been proposed based on junction temperature fluctuation characteristics, revealing the coupling mechanism between thermal cycling and device aging [13]. In medium-voltage scenarios such as locomotive traction, high power density and frequent load switching further exacerbate reliability challenges. It's indicated that power device failures in traction converters are directly associated with abrupt temperature variations during start-stop phases, whereas fatigue degradation is accelerated by dc-bus voltage fluctuations through electrothermalmechanical coupling effects [14]. In [15], a real-time operational condition-based reliability evaluation method is reported, and a traction converter lifetime prediction platform is established via online loss–junction temperature

Received 6 May 2025; revised 2 July 2025; accepted 17 July 2025. Date of publication 22 July 2025; date of current version 23 December 2025. This work was supported by China Southern Power Grid Company Technology Project under Grant 030400KK52222021. Recommended for publication by Associate Editor H. Iu. *(Corresponding author: Jun Jiang.)*

Jun Jiang and Beibei Chen are with the Jiangsu Key Laboratory of New Energy Generation and Power Conversion, Nanjing University of Aeronautics and Astronautics, Nanjing 211106, China (e-mail: jiangjun0628@nuaa.edu.cn; sx2303109@nuaa.edu.cn).

Qingwei Zhu is with the Ningbo Shenglong Automotive Powertrain System Company Ltd., Ningbo 315104, China (e-mail: qw.zhu@sheng-long.com).

Xuefeng Duan is with the Jiangsu Fulehua Semiconductor Technology Company Ltd., Yancheng 224200, China (e-mail: duanxf@ftpowersemi.com).

Renli Fu is with the School of Materials Science and Technology, Nanjing University of Aeronautics and Astronautics, Nanjing 211106, China (e-mail: renlifu@nuaa.edu.cn).

Color versions of one or more figures in this article are available at https://doi.org/10.1109/TPEL.2025.3591642.

Digital Object Identifier 10.1109/TPEL.2025.3591642

computation and rain-flow counting models. In high-voltage flexible dc systems, modular multilevel converter (MMC) has become the dominant topology, and the reliability depends on submodule operational conditions and redundancy design. Device failure mechanisms are explained and verified by developing an MMC reliability model that incorporates high voltage/high power operational scenarios, and the vulnerabilities are systematically identified [16]. The nonlinear impact of redundancy on system reliability is quantified through a multicomponent coupling model that integrates power devices, capacitors, and thermal management [17]. Reliability model of specific scenarios and equipment have been evaluated, but it is difficult to be directly transferred to PET system due to the complex integration of multistage power conversion units, including ac/dc, dc/ac, and high-frequency isolation.

For PET systems with their unique multistage conversion architectures, existing research has primarily focused on the impacts of power electronic topologies and redundancy designs on reliability. Device losses are calculated based on operational characteristics across different stages, the distribution of junction temperature in multitime scale components is analyzed, and reliability levels under varying operating modes are specifically evaluated for MMC-based PET [18]. Furthermore, researchers have proposed a failure rate calculation method incorporating redundancy design, establishing a reliability model for multiport cascaded PET systems [19]. While these efforts focus on the reliability evaluation of power electronics, the HFT is neglected, the critical component in the system. Under high-frequency and high-*dv/dt* electrical stress, the synergistic effects of partial discharge and dielectric loss-induced heating in HFT insulation materials lead to cumulative electro-thermal damage, accelerating insulation failure and significantly shortening insulation lifespan, which constrains the long-term stable operation of PET [20]. Agarwal et al. [21] analyzes the influence of high-frequency square wave voltage frequency and *dv/dt* on the lifespan of typical HFT insulation materials, indicating that insulation lifespan decreases with increasing frequency and *dv/dt*. Specifically, when frequency increases from 10 to 50 kHz, the insulation lifespan was reduced by 90%. The synergistic effects of frequency and temperature are further considered. The breakdown voltage characteristics of epoxy resin under operational frequencies of 0.5–8 kHz and temperatures of 30°C –120°C are investigated. Experimental results demonstrate that both increasing frequency and temperature reduce insulation breakdown voltage, with frequency playing a more dominant role [22]. Current studies mainly focus on the insulation materials, emphasizing the characteristics under different parameters, but fail to account for the impact of insulation lifespan on PET systems. Moreover, there is a lack of comprehensive analysis integrating the combined effects of power electronic topologies and HFT insulation characteristics on the overall reliability of PET equipment.

Therefore, the comprehensive reliability assessment model for PET systems that considers both power electronic devices and HFT insulation is proposed. Initially, an enhanced analytical model for component losses is established by considering the topology and operational characteristics of PETs. The module junction temperature distribution is obtained by using the Foster thermal network model. The failure rate is analyzed by combining the reliability assessment criteria. Second, considering the insulation system as a critical weak point in HFT unit, interlayer insulation lifespan and reliability are investigated through HFT prototype testing. A multistage PET reliability assessment model is developed accounting for the series-parallel connection among components in the topology. Finally, the effectiveness of the model is verified through specific case studies, and the impact of switching frequency on PET reliability is analyzed. The research results provide a theoretical basis for the optimized design and operational maintenance of PET, while also contributing to the improvement of future distribution network reliability and stability.

II. Typical Structure of MMC-Based Medium-Voltage Power Electronic Transformer

The input stage of ac/dc PETs is primarily divided into two structures: one based on the MMC and the other on the cascaded H-bridge. The MMC-based PETs require fewer switching components and HFTs, has a relatively lower cost [23], and has been more widely adopted in demonstration projects. Therefore, our work takes MMC-type PET as a typical example to model and analyze the reliability of the PET system. As shown in Fig. 1, the topology of an MMC-based PET system includes the rectification stage, the dual active bridge (DAB) isolation stage, and the inversion stage, forming three subsystems: the input stage, the isolation stage, and the isolation stage.

1) The input stage adopts a MMC as the rectifier, using submodules (SMs) as the basic power units. The SM adopts a half-bridge topology, consisting of two IGBT modules. The working states of the SMs can be categorized into locked, turned ON, and turned OFF. In the turned-ON state, the upper switch is turned ON and the lower switch is turned OFF. The capacitor is charged and discharged. The upper bridge arm IGBT and the lower bridge arm antiparallel diode are in a complementary relationship.
2) The isolation stage adopts DABs as the dc–dc link. The typical nonresonant DAB topology consists of three l stages, including two H-bridges and a HFT. Each DAB unit includes eight IGBT modules.
3) The isolation stage is the three-phase inverter stage, with IGBT modules in each bridge arm.

III. Losses and Junction Temperature Analysis of Power Electronic Transformer

The operating conditions directly determine the losses of the power electronic components, which mainly include IGBT on-state losses and switch losses, diode on-state losses and reverse recovery losses.

A. Component Losses Calculation

Figs. 2 and 3 show the voltage, current, and power waveforms of the IGBT and diode in different operating states. In Fig. 2, I_c represents the current flowing through the IGBT,

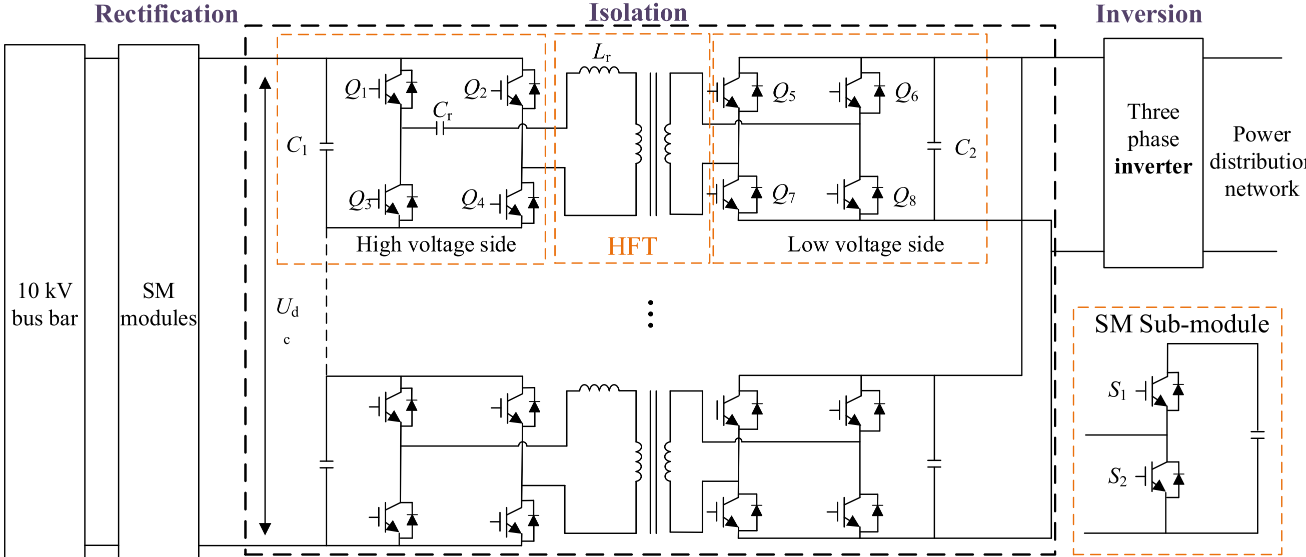

Fig. 1. MMC-based PET topology.

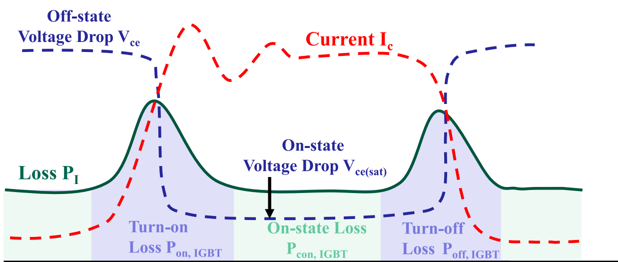

Fig. 2. IGBT loss waveform.

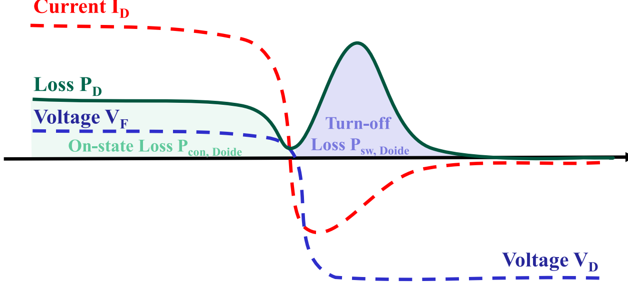

Fig. 3. Diode loss waveform.

$P_{\text{on, IGBT}}$, $P_{\text{off, IGBT}}$, and $P_{\text{con, IGBT}}$ represent the turn-ON, turn-OFF, and ON-state losses of the IGBT, and V_{ce} and $V_{ce,set}$ represent the OFF-state and ON-state voltage drop. In Fig. 3, I_D represents the current flowing through the diode, V_F and V_D is the ON-state voltage and turn-OFF voltage. $P_{\text{con, Doide}}$ and $P_{\text{sw, Doide}}$ are the ON-state and turn-OFF losses of the diode.

Due to the influence of the ON-state resistance and PN junction potential in the IGBT, the IGBT in the ON-state maintain a certain saturation voltage drop $V_{ce(sat)}$, which together with the ON-state current I_c produces the ON-state loss. The ON-stage losses of IGBT can be calculated using (1). The ON-stage losses of diode can be expressed by (2)

$$P_{\text{con,IGBT}} = V_{\text{ce(sat)}} I_c + \mathrm{r}_0 I_c^2 \tag{1}$$

$$P_{\text{con,Doide}} = V_F I_D + \mathrm{r}_D I_D^2 \tag{2}$$

where r_0 is the ON-state resistance of the IGBT and r_D is the ON-state resistance of the diode.

When the IGBT operates in the switching mode, there will be a period of overlap between the voltage and current waveforms during the turn-ON and turn-OFF transient processes, resulting in switch losses. Additionally, due to the tail current during the turn-OFF process, the turn-OFF losses of the IGBT are larger than the turn-on losses during the overlap time. The switch losses of the IGBT can be expressed as

$$P_{\text{sw}} = f_{\text{sw}} E_{\text{sw}} \tag{3}$$

$$E_{\text{sw}} = E_{\text{on}} + E_{\text{off}} \tag{4}$$

$$P_{\text{sw,IGBT}} = f_{\text{sw}} E_{\text{off}}^{\text{typ}} \frac{U_C I_C}{U_{\text{CE0}} I_{\text{CE0}}} \tag{5}$$

where f_{sw} is the switching frequency; E_{sw} is the energy losses of IGBT one switch cycle. E_{off}^{typ} is the IGBT turn-OFF loss under rated operating conditions. U_{CE0} and I_{CE0} are the voltage and current under rated conditions, which can be found in the device datasheet.

The diode has fast recovery characteristics, and its turn-ON losses can be considered negligible compared to the reverse recovery losses (less than 1%). When the diode is turned OFF, the recovery of its reverse blocking capability requires a transitional period, during which the current flowing through the diode overlaps with its terminal voltage, resulting in reverse recovery losses. This can be expressed as

$$P_{\text{sw,Doide}} = f_{\text{sw}} E_{\text{ref}} \frac{U_D I_D}{U_{\text{CE0}} I_{\text{CE0}}} \tag{6}$$

where E_{ref} is the reverse recovery losses of diode one switch cycle.

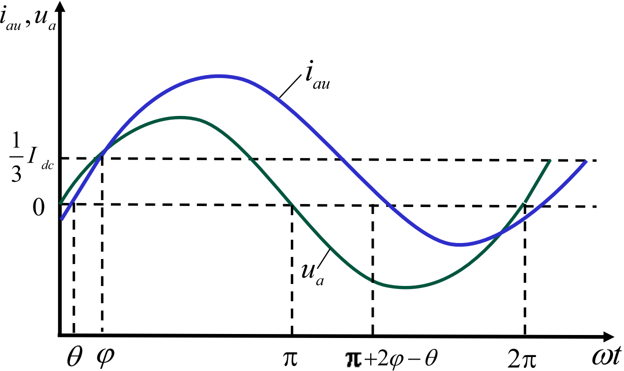

Fig. 4. Phase *a* of output voltage and upper bridge arm current.

1) Component Losses of MMC Rectification Stage: In the MMC, all SMs in each bridge arm are periodically switched according to certain rules and stacked to form a nearly sinusoidal output voltage. The bridge arm current contains two parts, one is the dc current flowing from the positive dc bus to the negative dc bus, and the other is the ac phase current distributed in the upper and lower bridge arms. Ideally, the dc current is equally distributed among the three-phase units, and the ac phase current is equally distributed in the upper and lower bridge arms. The situation is similar for each phase in a three-phase system. For simplicity, the analysis is conducted using phase a as an example, as shown in Fig. 4. The phase voltage u_{a} and phase current i_{au} can be expressed as

$$\begin{cases} u_a = U_m \sin(\omega t) \\ i_{au} = I_m \sin(\omega t - \varphi) \end{cases} \tag{7}$$

where U_m and I_m are the amplitude of ac output voltage and current, I_{dc} is the dc current, ω is the fundamental angular frequency, and φ (power factor angle) is the phase difference between the ac output voltage and current of phase a.

If the double-frequency circulating current and other harmonic components in the bridge arm current are ignored, bridge arm current of each phase consists of a dc component and a fundamental frequency ac component. The upper and lower bridge arm currents, i_{au} and i_{al}, of phase a can be represented as the following equations [24]:

$$\begin{cases} i_{\mathrm{au}} = \frac{1}{3} I_{\mathrm{dc}} + \frac{1}{2} i_a \\ i_{\mathrm{al}} = \frac{1}{3} I_{\mathrm{dc}} - \frac{1}{2} i_a \end{cases}. \tag{8}$$

Assuming that the losses of the inverter are neglected, power balance gives

$$U_{\mathrm{dc}} I_{\mathrm{dc}} = \frac{3}{2} U_m I_m \cos\varphi. \tag{9}$$

According to Kirchhoff's voltage law, the duty ratios n_{au} and n_{al} for the upper and lower SMs of phase a are as follows:

$$\begin{cases} n_{\mathrm{au}} = \frac{1}{2}\left(1 - m\sin(\omega t)\right) \\ n_{\mathrm{al}} = \frac{1}{2}\left(1 + m\sin(\omega t)\right) \end{cases} \tag{10}$$

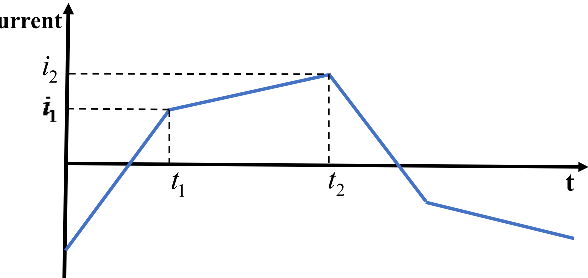

Fig. 5. DAB current waveform.

where *m* is the modulation ratio, and m $= 2U_m/U_{\mathrm{dc}}$. Thus, the currents in SMs S_1 and S_2 can be calculated as

$$\begin{cases} i_{S1} = n_{\mathrm{au}} i_{\mathrm{au}} = \frac{1}{2}\left(1 - m\sin(\omega t)\right) i_{\mathrm{au}} \\ i_{S2} = n_{\mathrm{al}} i_{\mathrm{al}} = \frac{1}{2}\left(1 + m\sin(\omega t)\right) i_{\mathrm{al}} \end{cases}. \tag{11}$$

In order to better estimate the thermal stress of the fully controlled devices in the inverter, the current stress in IGBT T_1 and T_2, as well as diodes D_1 and D_2, must be calculated separately. The upper bridge arm current waveform crosses zero at phase angles θ, $\pi+2\varphi$-θ, and $2\pi+\theta$, respectively. Since the devices only allow one-way current flow, the effective operating range for T_1 and D_2 is ($\pi+2\varphi$-θ, $2\pi+\theta$], and for T_2 and D_1 is (θ, $\pi+2\varphi$-θ]. Equations (12) and (13) can be used to calculate the average value and RMS value of the T_1 current

$$i_{\mathrm{avgT1}} = \frac{1}{2\pi}\int_{\pi+2\varphi-\theta}^{2\pi+\theta} \frac{1}{2}\left(1 - \mathrm{m}\sin(\omega \mathrm{t})\right) \cdot \left(\frac{I_{\mathrm{dc}}}{3} + \frac{I_m}{2}\sin(\omega t - \varphi)\right) d(\omega t) \tag{12}$$

$$i_{\mathrm{rmsT1}}^2 = \frac{1}{2\pi}\int_{\pi+2\varphi-\theta}^{2\pi+\theta} \frac{1}{2}\left(1 - \mathrm{m}\sin(\omega \mathrm{t})\right) \cdot \left(\frac{I_{\mathrm{dc}}}{3} + \frac{I_m}{2}\sin(\omega t - \varphi)\right)^2 d(\omega t). \tag{13}$$

2) Component Losses in the DAB Isolation Stage: The current in the DAB subsystem is a trapezoidal waveform, as shown in Fig. 5 for a voltage conversion ratio $k<1$. The expression for this current waveform is given by

$$\begin{cases} i_{S1} = n_{\mathrm{au}} i_{\mathrm{au}} = \frac{1}{2}\left(1 - m\sin(\omega t)\right) i_{\mathrm{au}} \\ i_{S2} = n_{\mathrm{al}} i_{\mathrm{al}} = \frac{1}{2}\left(1 + m\sin(\omega t)\right) i_{\mathrm{al}} \end{cases}. \tag{14}$$

According to the symmetry of the current waveform, the expression can be written as

$$\begin{cases} i_1 = \frac{U_1}{4 f_{\mathrm{sw}} L_s}\left[1 + (2D - 1)k\right] \\ i_2 = \frac{U_1}{4 f_{\mathrm{sw}} L_s}\left[2D - 1 + k\right] \end{cases} \tag{15}$$

where i_1 and i_2 are the current values at times t_1 and t_2; D is the phase-shift ratio of the H-bridge on the primary and secondary sides of the HFT (ranging from 0 to 1); f_{sw} is the switching frequency; L_s is the inductance value (480 μH in this case); U_1 is the voltage on the primary side of the HFT; and n is the turns ratio of the transformer. Consequently, the average value and

RMS value of the current for each semiconductor device within the switching cycle can be obtained.

Based on the above derivation, the expression for the transmitted power P can be further solved as

$$P = \frac{kU_1^2}{2f_{\text{sw}}L_{\text{s}}}D\left(1-D\right). \tag{16}$$

Conduction losses

$$P_{\text{con}} = V_0 i_{\text{avg}} + R_0 i_{\text{rms}}^2 \tag{17}$$

where V_0 and R_0 are IGBT or diode conduction characteristic curve fitting parameters.

Since the reverse parallel diodes in the DAB operate in natural commutation mode and their losses can be neglected, and the turn-ON losses of the diodes are small and can be ignored. The turn-ON action of the IGBT occurs in natural commutation mode as well. Therefore, the losses of the power device modules within the switching cycle are mainly caused by the turn-OFF of the IGBT

$$\begin{aligned} P_{\text{sw},S_1} &= f_{\text{sw}}E_{\text{off}} = \frac{U_1 i_2}{U_{\text{CE0}}I_{\text{CE0}}}f_{\text{sw}}E_{\text{typ}}^{\text{off}} \\ P_{\text{sw},S_5} &= f_{\text{sw}}E_{\text{off}} = \frac{nU_2 i_1}{U_{\text{CE0}}I_{\text{CE0}}}f_{\text{sw}}E_{\text{typ}}^{\text{off}} \end{aligned} \tag{18}$$

where E_{off} is the turn-OFF loss of the IGBT under rated conditions, and U_{CE0} and I_{CE0} are the voltage and current under rated conditions, respectively, which can be found in the device datasheet.

3) Component Losses in Three-Phase Inversion Stage: There has been extensive research on the calculation of losses in three-phase inverter circuits, and the expressions for conduction losses and switching losses are as follows [25], [26]:

$$\begin{cases} P_{\text{IGBT}} = \frac{f_{\text{sw}}E_{\text{sw}}U_{\text{dc}}I_m}{U_{\text{CE0}}I_{\text{CE0}}} + U_0 I_m\left(\frac{1}{2\pi}+\frac{M\cos\alpha}{8}\right) \\ \qquad +R_{ce}I_m^2\left(\frac{1}{8}+\frac{M^2\cos\alpha}{3\pi}\right) \\ P_{\text{Doide}} = \frac{f_{\text{sw}}E_{\text{rec}}U_{\text{dc}}I_m}{U_{\text{CE0}}I_{\text{CE0}}} + U_0 I_m\left(\frac{1}{2\pi}-\frac{M\cos\alpha}{8}\right) \\ \qquad +R_D I_m^2\left(\frac{1}{8}-\frac{M^2\cos\alpha}{3\pi}\right) \end{cases} \tag{19}$$

where E_{sw} represents the energy loss during IGBT turn-OFF, E_{rec} represents the reverse recovery loss of the diode, I_m is the amplitude of the three-phase current, U_{dc} is the dc voltage, M is the three-phase pulsewidth modulation index, U_0 represents the voltage drop across the devices during conduction, α is the power factor angle, and R_{ce} and R_D represent the conduction resistances of the IGBT and diode.

B. Component Junction Temperature Evaluation

According to the thermal-electric analogy theory, the thermal characteristics of IGBT modules can be described by an RC equivalent network. Among the thermal parameters, thermal resistance, thermal capacitance, temperature, and power (heat flow) can be analogized to resistance, capacitance, voltage, and current in electricity, respectively. Therefore, the thermal characteristics of power devices can be described by the Foster network. Fig. 6 shows the thermal impedance curve of power devices, the corresponding Foster thermal network, and its corresponding parameters at all levels

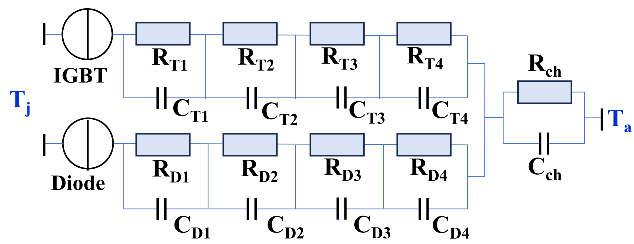

Fig. 6. Foster thermal network model.

$$T_{\text{j}} = \left(Z_{jc} + Z_{\text{ch}}\right)P_{\text{loss}} + T_a \tag{20}$$

$$\begin{cases} Z_{jc}(t) = \sum_{\text{i}=1}^{n} R_i\left(1-e^{-t/R_iC_i}\right) \\ Z_{\text{ch}}(t) = R_{\text{ch}}\left(1-e^{-t/R_{\text{ch}}C_{\text{ch}}}\right) \end{cases}. \tag{21}$$

T_{j} is the steady-state junction temperature of the device, Z_{jc} is the thermal impedance from the chip of IGBT / Diode to the copper substrate; Z_{ch} is the thermal impedance from the copper substrate of IGBT / Diode to the heat sink. P_{loss} is the average power loss over the device's switching period. The parameters R_i and C_i correspond to the n-order thermal impedance components between the junction and case, whereas, R_{ch} and C_{ch} characterize the thermal impedance from case to heatsink. T_a indicates the heatsink temperature.

The time constant of the heat sink is generally on the order of tens of seconds to minutes. For short-term reliability analysis, this is a relatively long process. Therefore, it can be considered that under a short time scale, the temperature of the heat sink has no time to change, that is, it can be regarded as constant. To ensure its reliability, the temperature of the heatsink can be selected as the temperature under the worst working condition, which is set at 50°C.

C. Component Failure Rate Analysis

The MIL-HDBK-217 guideline is the basis for the reliability assessment of civilian power electronic equipment. This reliability assessment model adopts the stress analysis method, taking the product of the acceleration factor and the basic failure rate as the basic form of failure rate assessment. According to MIL-HDBK method, the failure rate for an IGBT module is as follows:

$$\lambda = \lambda_b \pi_S \pi_C \pi_Q \pi_E \pi_T \tag{22}$$

where λ_b is the basic failure rate, π_{S} is the electrical stress acceleration factor, related to the actual operating overvoltage level. π_{C} is the structural impact factor, related to the materials and structure of the IGBT. π_Q is the quality management level impact factor. π_E is the environmental impact factor, related to the natural environment of operation, including pollution level; The values of each parameter are given in Table I [27], [28]. The thermal stress acceleration factor π_T is related to the junction temperature level during operation, and can be

TABLE I
VALUES FOR EACH PARAMETER

	λ_b	π_S	π_C	π_Q	π_E
IGBT	0.012	3.49	1	5.5	6
Diode	0.064	0.06	1	5.5	6

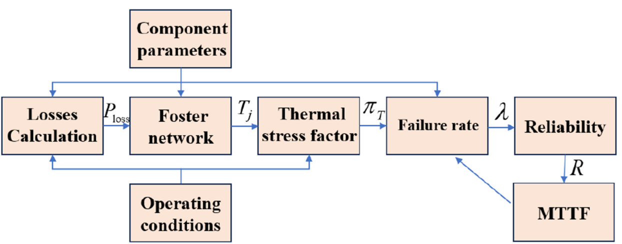

Fig. 7. Reliability assessment flowchart for power electronic devices.

specifically expressed as

$$\pi_T = \alpha e^{\left[\beta\left(\frac{1}{293} - \frac{1}{T_j + 273}\right)\right]} \tag{23}$$

where T_j is the average junction temperature of the IGBT under steady-state operation, and α, β are constants with specific values varying for different components. $\alpha = 1$ and $\beta = 8122.8$ for IGBTs and diodes, while $\alpha = 0.85$ and $\beta = 4641.6$ for capacitors [27], [28].

IV. POWER ELECTRONIC TRANSFORMER RELIABILITY ANALYSIS

For a power electronic device or a specific electrical equipment module, its failure is considered as an accidental event, hence its failure rate is constant, and the reliability can be calculated as

$$R(t) = e^{-\lambda t}. \tag{24}$$

The average of mean time to failure (MTTF) can be obtained as

$$\text{MTTF} = \int_0^\infty R(t)dt = \frac{1}{\lambda}. \tag{25}$$

The overall process of reliability assessment for power electronic devices is shown in Fig. 7. The diagram illustrates the data transmission flow of a full-chain computational model spanning from current distribution to system lifetime evaluation. Specifically, it begins with an analysis of the operating current waveforms of IGBTs and diodes to establish a precise loss model incorporating both conduction and switching losses. Next, the Foster thermal network model is employed to convert power losses into junction temperature distributions. Combined with the MIL-HDBK-217 standard, this enables the quantitative assessment of failure rates by linking junction temperature to thermal stress factors. Finally, the model completes the multilevel system lifetime evaluation through the interconversion of failure rate, reliability, and lifespan.

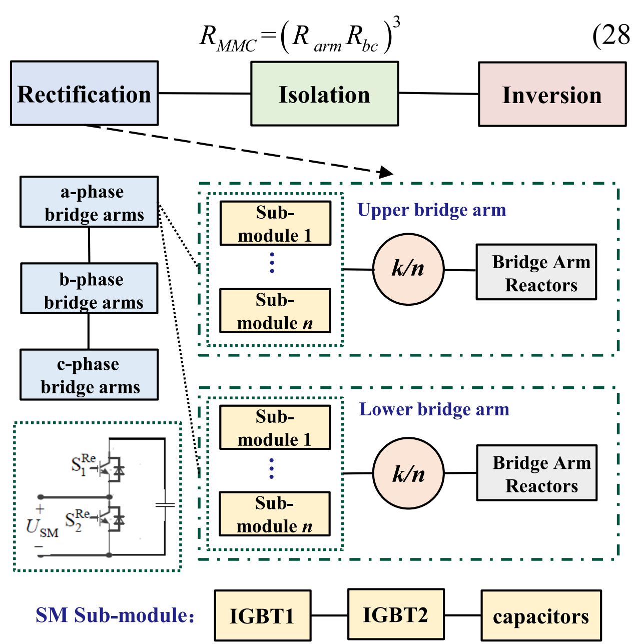

Fig. 8. MMC rectification stage reliability assessment model.

A. MMC Rectification Stage Reliability Calculation

First, the SMs of the MMC module are modeled for reliability. Taking a half-bridge SM as an example, it includes two antiparallel diodes IGBTs, a driver circuit, capacitors, and a charging power supply. If any component fails, the SM will also fail, therefore the reliability assessment model is depicted in Fig. 8.

According to reliability principles, the reliability of the MMC half-bridge SM is calculated as follows:

$$R_{\text{SM}} = (R_{\text{IGBT}})^2 R_C R_{PS} R_{SC} \tag{26}$$

where R_{IGBT}, R_c, R_{PC}, R_{SC} represent the reliabilities of the IGBT module, capacitor, charging power supply, and driver circuit, respectively.

Assuming each bridge arm consists of n SMs and considering redundancy, the bridge arm can operate normally when no less than *k* SMs are functioning, and fails when more than (n-k) SMs are faulty. The reliability of the bridge arm is evaluated using an *n*-out-of-*k* voting system reliability model, and the reliability function of a single-phase bridge arm is

$$R_{\text{arm}} = \sum_{i=k}^{n} \begin{bmatrix} n \\ i \end{bmatrix} (R_{\text{SM}})^i (1 - R_{\text{SM}})^{n-i}. \tag{27}$$

Considering the reliability function of the valve base controller as R_{bc}, the reliability function of the three-phase MMC section is

$$R_{\text{MMC}} = (R_{\text{arm}} R_{\text{bc}})^3. \tag{28}$$

B. Isolation Stage Reliability Calculation

Inside the isolation stage, assuming there are n DAB modules in parallel, it can be considered that the DAB isolation stage can work properly when no less than k DAB modules are operating

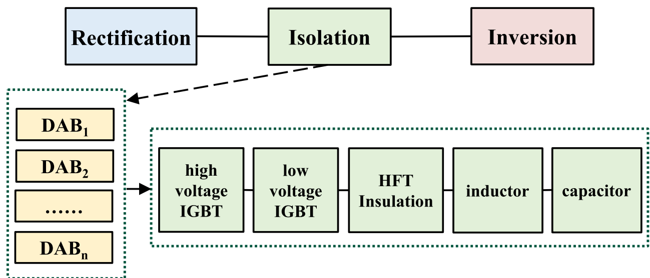

Fig. 9. DAB isolation stage reliability model.

normally. Therefore, the reliability assessment model for the isolation stage is illustrated in Fig. 9.

The reliability of the isolation stage and a single DAB module is as follows:

$$R_{\text{ISO}} = \sum_{i=k}^{n} \begin{bmatrix} n \\ i \end{bmatrix} R^{i}{}_{\text{DAB}} \cdot \left[1 - R^{i}{}_{\text{DAB}}\right]^{n-i} \tag{29}$$

$$R_{\text{DAB}} = R_{\text{HFT}} \cdot R^{4}{}_{H_IGBT} \cdot R^{4}{}_{L_IGBT} \cdot R_{Cr} \cdot R_{Lr} \cdot R_{C}^{2} \tag{30}$$

where R_{iso} is the reliability of the isolation stage, R_{H_IGBT} is the reliability of the high-side IGBT, R_{L_IGBT} is the reliability of the low-side power device, R_{HFT} is the reliability of HFT, and R_C, R_{Cr}, R_{Lr} represent the reliabilities of the stabilizing capacitor, resonant capacitor, and resonant inductor.

For HFTs, the weak point primarily lies in the insulation system, particularly the interlayer insulation, which is subjected to the most severe electrical stress. When defects occur in the windings, they can damage the interlayer insulation and expand the defect area, thereby affecting the overall lifespan and reliability of the HFT. It is generally believed that the interlayer insulation subjected to the highest stress is the first to fail, leading to transformer damage. Assuming that the interlayer insulation under the highest stress in the HFT consists of n_H layers, each with a reliability of R_i (where $i = 12\ldots, n_H$), the overall reliability of the transformer can be expressed as follows:

$$R_{\text{HFT}} = R_1 \cdot R_2 \ldots \cdot R_{n_H}. \tag{31}$$

C. Isolation Stage Reliability Calculation

The inverter stage consists of 6 IGBT modules with the reliability expressed as

$$R_{\text{INV}} = (R_{\text{IGBT}})^6. \tag{32}$$

D. Power Electronic Transformer Reliability Calculation

Any failure in the rectification stage, DAB isolation stage, or inverter stage of the system will lead to PET system failure, thus can be viewed as a series reliability system

$$R_{\text{PET}} = R_{\text{MMC}} R_{\text{ISO}} R_{\text{INV}}. \tag{33}$$

V. Case Analysis

The case aims to evaluate the reliability of the PET and its components under operational conditions. The operating parameters of the PET are as follows: The rated capacity of the MMC-type PET is 10 kW, 10 kV/380 V, and the HFT operates at a rated frequency of 20 kHz. The IGBT modules used in the MMC rectification stage and DAB isolation stage are 5SNA 0800N330100 with a voltage design of 1900 V. 10 SMs are required for both rectification stage and DAB isolation stage. The inversion stage IGBT modules used are 5SNA 3600E170300.

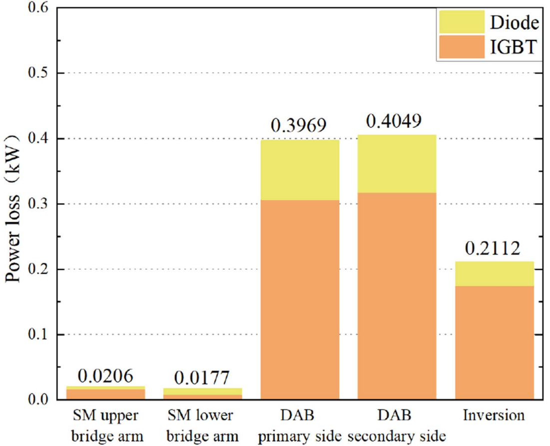

Fig. 10. IGBT modules power loss in each stage.

TABLE II
IGBT Modules Junction Temperature in Each Stage (°C)

IGBT Modules in Each Stage	IGBT	Diode
SM upper bridge arm	50.41	50.20
SM lower bridge arm	50.21	50.46
DAB primary side	57.59	51.47
DAB secondary side	57.88	51.42
Inversion	52.87	51.62

A. IGBT Module Losses and Junction Temperature Analysis

When transmitting the same power, the IGBT losses in the various conversion stages of PET are different. In the above case study, the loss situation of each module can be obtained as shown in Fig. 10.

Due to lower power transmission, the IGBT losses in the rectification and inversion stages are relatively low. Specifically, in the rectification stage located on the high-voltage side, operating at higher voltage than the inversion stage, the equivalent current passing through each IGBT module in the inverter stage is larger, resulting in higher IGBT losses in the inversion stage compared to the rectification stage. Additionally, the high switching frequency (20 kHz) in the DAB stage leads to relatively higher IGBT losses.

Based on the loss results in Fig. 10, the junction temperature of each stage's IGBT modules is calculated as given in Table II.

It is evident that higher component losses correspond to higher junction temperatures, with the DAB isolation stage having the highest temperature, followed by the inversion stage and then the MMC rectification stage. This is mainly due to the high

TABLE III
ANNUAL FAILURE RATES OF IGBT MODULES IN EACH STAGE

IGBT Modules in Each Stage	Failure Rate (times/year)		
	IGBT	Diode	Module
SM upper bridge arm	0.0009	0.0009	0.0018
SM lower bridge arm	0.0009	0.0009	0.0018
DAB primary side	0.0038	0.0010	0.0048
DAB secondary side	0.0039	0.0010	0.0049
Inversion	0.0015	0.0010	0.0025

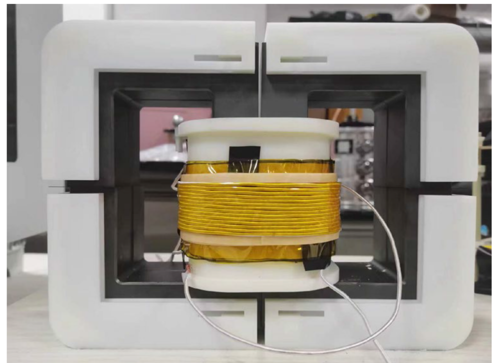

Fig. 11. Physical implementation of the HFT prototype.

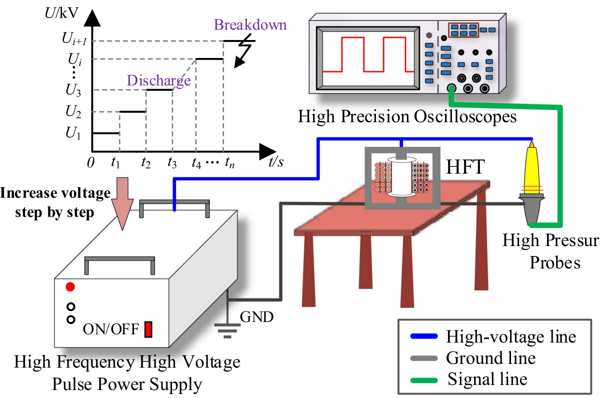

Fig. 12. HFT insulation lifespan test platform.

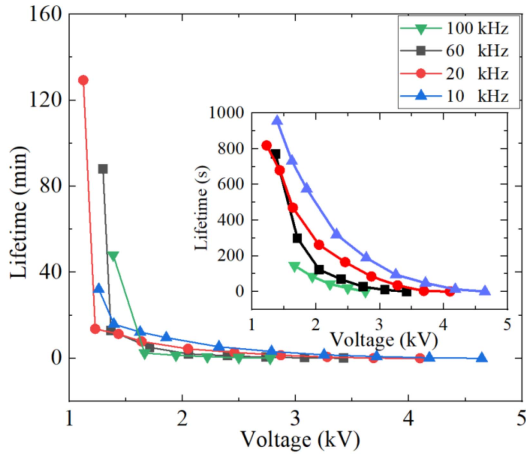

Fig. 13. Lifespan of interlayer insulation at different voltages and frequencies.

switching frequency in the DAB isolation stage, resulting in significantly higher switching losses than the IGBT modules in the MMC stage. The three-phase inversion stage has a low voltage and a high on-state current of the IGBT module. Therefore, it has a larger on-state loss than the components in the MMC stage.

B. IGBT Module Failure Rate Analysis

Based on the junction temperature analysis results, the annual equivalent failure rates of the IGBT modules in each stage are calculated as given in Table III. The DAB isolation stage's IGBT modules have the highest failure rates, with primary and secondary side failure rates of 0.0048 and 0.0049 times/year. The three-phase inversion stage has a failure rate of 0.0025 times/year. The SMs in the upper and lower bridge arms of the MMC have failure rates around 0.0018 times/year.

C. HFT Insulation System Reliability Analysis

For the interlayer insulation lifespan, breakdown tests under different pulsed voltage levels can be conducted on the HFT prototype. The physical implementation of the HFT prototype is illustrated in Fig. 11. The transformer windings adopt a concentric structure, with the low-voltage winding placed on the inner layer and the high-voltage winding on the outer layer. Polyimide insulating film is applied between layers to enhance dielectric strength.

Based on the transformer's structural, artificial defects were introduced into the windings of the prototype. A step-by-step voltage method was applied to conduct withstand voltage testing and lifetime evaluation of insulation defects in the HFT under pulsed voltage conditions, with the experimental setup detailed in Fig. 12. The experimental setup employed a pulse voltage with 50 ns rise time and 50% duty cycle, while varying the frequency from 10 to 100 kHz. Test voltages were applied at 25% to 100% of the breakdown voltage threshold (in 10% increments) under different parameter conditions. For each voltage level, five tests were conducted with replacement of PI film after each breakdown event. The insulation lifetime results under various voltage and frequency conditions are presented in Fig. 13. The data demonstrate that: at a given frequency, insulation lifetime progressively increases with decreasing voltage; at a fixed voltage level, higher frequencies result in shorter insulation lifetimes.

The voltage-lifetime (U-L) characteristics at different frequencies were effectively modeled using an inverse power function, with all fitted equations demonstrating excellent goodness-of-fit (R^2>0.8) as given in Table IV The regression analysis shows the constant term in the fitted equations increases with higher frequencies while the power exponent exhibits a corresponding decrease.

The insulation lifetime under different voltage and frequency conditions can be obtained by fitting experimental data, which is then converted into single-layer insulation reliability using (25),

TABLE IV
EQUATIONS FOR U-L VOLTAGE CHARACTERISTICS AT DIFFERENT FREQUENCIES

Frequency (kHz)	U-L characteristics (s)	R^2
10	$L(U)=8031.60\cdot U^{-4.51}$	0.84
20	$L(U)=7762.87\cdot U^{-5.31}$	0.88
60	$L(U)=17515.92\cdot U^{-7.01}$	0.93
100	$L(U)=48071.86\cdot U^{-9.57}$	0.90

TABLE V
FAILURE RATE OF COMPONENTS FROM REFERENCE

Individual components in Each Stage		Failure Rate (times/year)
Rectification stage	Capacitor	0.0017
	Drive Circuit	0.0014
	Power Supply	0.0350
DAB isolation stage	Capacitor	0.0176
	Drive Circuit	0.0003
	Power Supply	0.0143

TABLE VI
FAILURE RATE AND LIFESPAN ACROSS PET STAGES

	Failure Rate (times/year)	Lifespan (years)
SM Sub-Module	0.0417	23.98
Rectification	0.0848	11.79
Single DAB	0.1876	5.33
Isolation	0.6024	1.66
Inversion	0.0150	66.67
PET	0.7022	**1.42**

thereby enabling the calculation of the overall HFT reliability through (31).

D. PET System Reliability Analysis

In the MMC rectification stage and DAB isolation stage, the failure rates of IGBT modules are calculated using the algorithm proposed in this article. The failure rates of the capacitors, drive circuits, and power supplies can be obtained by referring to literature [17], [19], [25], as given in Table V.

The failure rates and lifespan across PET stages are calculated and given in Table VI. The DAB isolation stage exhibits the highest overall failure rate, representing the weakest link in the PET system. The MMC rectification stage, due to its higher component count, demonstrates the second-highest failure rate. Since the failure of any single component leads to system-wide dysfunction, the PET can be modeled as a series reliability system. The system failure rate and lifespan are calculated using (33), the MTTF of the PET system is 1.42 years.

By employing exponential distribution-based reliability models, the reliability variation curves of each stage in the PET are derived and illustrated in Fig. 14. In the PET system, the reliability of the inversion stage changes most slowly and has the longest life, while the isolation stage reliability function decreases the fastest with the shortest life.

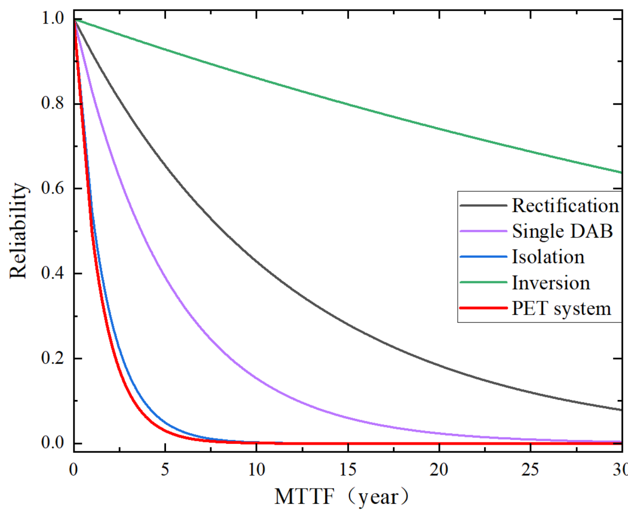

Fig. 14. Reliability variation of different stages in PET.

TABLE VII
COMPARISON BETWEEN OUR WORK AND PREVIOUS STUDIES

Study	Research target	Lifetime (years)	Limitations/Advantages
Wang et al. [17]	Converter （200 MW）	1.3782	Only the converter is considered
Cheng et al. [18]	MMC-based PET（2 MW）	1.0014	HFT was not considered
Yang et al. [19]	MMC-based PET（2 MW）	0.7	HFT was not considered
Our work	MMC-based PET	1.42	Unified co-modeling of power devices & HFT insulation

The model developed in this article innovatively incorporates both power electronic devices and HFT insulation into a unified framework for coordinated analysis. It precisely models the electrothermal stress of power devices, such as IGBTs under complex operating conditions through current-loss-junction temperature networks, while also quantifying the aging process of HFT insulation under high-voltage and high-frequency conditions via experimentally established voltage-lifetime models. A comparison between this article and previous studies is given in Table VII.

The loss of power electronic devices is closely related to the switching frequency. Changing the switching frequency of the isolation stage affects the reliability and life of PET, as shown in Fig. 15. An increase in switching frequency leads to elevated power losses and higher failure rates in the isolation stage of the DAB, consequently reducing the overall lifespan of the PET system.

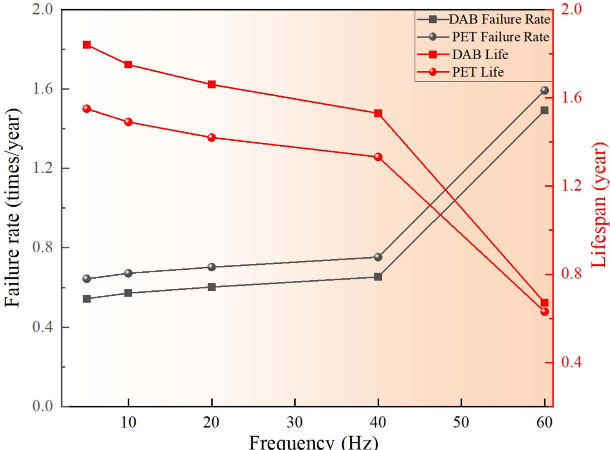

Fig. 15. Reliability and lifespan variation of PET at different frequencies.

V. Conclusion

A reliability model of the PET is developed in this article, where operational condition-dependent component failure rates are rigorously integrated. Based on the theoretical and practical case analysis, the key findings are concluded as follows.

1) For the PET system, the higher the component losses, the higher the junction temperature and failure rate. The overall failure rate of the DAB stage is the highest among the different three main power conversion stages forming a MMC-PET, making it the weak link in the PET system. Due to large number of components used in the MMC rectification stage, its failure rate is second only to that of the DAB inversion stage.
2) The insulation lifespan characteristics of the HFT under typical operating conditions were investigated. A prototype HFT with a rated frequency of 20 kHz was developed and tested to study the withstand time of internal defects at different voltage levels, and the inverse power law was used to establish the voltage-life (U-L) characteristic equation. This enabled the construction of a lifespan assessment model for the HFT's multilayer insulation.
3) Based on the constructed reliability assessment model for PETs, the MTTF of the PET equipment under 10 kW/20 kHz HFT prototype is calculated as 1.42 years. An increase in switching frequency leads to elevated power losses and higher failure rates in the isolation stage of the DAB, consequently reducing the overall lifespan of the PET system.

Based on the aforementioned research analysis, the service life of PET systems can be effectively enhanced through the following measures: reducing DAB switching frequency, optimizing HFT insulation design, implementing redundant configurations, and improving thermal management systems. The current model validation is limited to laboratory-scale case studies under controlled conditions, and future research will focus on field verification and optimization of PET thermal design.

References

[1] O. Azeem et al., "A comprehensive review on integration challenges, optimization techniques and control strategies of hybrid AC/DC microgrid," *Appl. Sci.*, vol. 11, no. 14, Jul. 2021, Art. no. 6242.

[2] J. Zhang, J. Liu, J. Yang, N. Zhao, Y. Wang, and T. Q. Zheng, "A modified DC power electronic transformer based on series connection of full-bridge converters," *IEEE Trans. Power Electron.*, vol. 34, no. 3, pp. 2119–2133, Mar. 2019.

[3] W. Yi and X. Wang, "Research on power electronic transformer based day-ahead economic operation strategy of AC/DC hybrid distribution network," *Modern Elect. Power*, vol. 38, no. 3, pp. 339–345, Jun. 2021.

[4] M. H. M. Sathik, P. Sundararajan, F. Sasongko, J. Pou, and S. Natarajan, "Comparative analysis of IGBT parameters variation under different accelerated aging tests," *IEEE Trans. Electron Devices*, vol. 67, no. 3, pp. 1098–1105, Mar. 2020.

[5] T. Ahmad, R. Madonski, D. Zhang, C. Huang, and A. Mujeeb, "Data-driven probabilistic machine learning in sustainable smart energy/smart energy systems: Key developments, challenges, and future research opportunities in the context of smart grid paradigm," *Renew. Sustain. Energy Rev.*, vol. 160, May 2022, Art. no. 112128.

[6] M. Hernes, S. D'Arco, A. Antonopoulos, and D. Peftitsis, "Failure analysis and lifetime assessment of IGBT power modules at low temperature stress cycles," *IET Power Electron.*, vol. 14, no. 7, pp. 1271–1283, Apr. 2021.

[7] C. Zhan et al., "Wear out mechanism of press-pack IGBTs under accelerated aging test," *IEEE J. Emerg. Sel. Topics Power Electron.*, vol. 10, no. 5, pp. 5132–5141, Oct. 2022.

[8] Y. Zhang et al., "Influence of the uneven temperature distribution on the electrode warpage of PP IGBTs," *IEEE Trans. Power Electron.*, vol. 38, no. 4, pp. 5296–5308, Apr. 2023.

[9] J. L. Afonso et al., "A review on power electronics technologies for power quality improvement," *Energies*, vol. 14, no. 24, Dec. 2021, Art. no. 8585.

[10] X. Xu, T. Wang, L. Mu, and J. Mitra, "Predictive analysis of microgrid reliability using a probabilistic model of protection system operation," *IEEE Trans. Power Syst.*, vol. 32, no. 4, pp. 3176–3184, Jul. 2017.

[11] V. Monteiro, J. S. Martins, J. C. Aparício Fernandes, and J. L. Afonso, "Review of a disruptive vision of future power grids: A new path based on hybrid AC/DC grids and solid-state transformers," *Sustainability*, vol. 13, no. 16, Aug. 2021, Art. no. 9423.

[12] K. Ma, M. Liserre, F. Blaabjerg, and T. Kerekes, "Thermal loading and lifetime estimation for power device considering mission profiles in wind power converter," *IEEE Trans. Power Electron.*, vol. 30, no. 2, pp. 590–602, Feb. 2015.

[13] L. Zhang and J. Wei, "Module lifetime evaluation method for the power converter of the DFIG based on the analysis of the field wind speed probability and ambient temperature," *IEEE Access*, vol. 10, pp. 72545–72556, 2022.

[14] L. Wang, M. Zhou, Z. Dongye, Y. Sha, and J. Chen, "A condition evaluation simplified method for traction converter power module based on operating interval segmentation," *Sensors*, vol. 23, no. 5, Feb. 2023, Art. no. 2537.

[15] Y. Shi, J. Liu, Y. Ai, S. Chen, and C. Pei, "Lifetime prediction method of the traction converter IGBT based on plastic strain energy density," *IEEE Trans. Transp. Electrific.*, vol. 10, no. 1, pp. 1286–1298, Mar. 2024.

[16] T. Zhang, M. Huang, L. Zhu, and X. Zha, "Reliability evaluation of MMC system considering working conditions," *J. Eng.*, vol. 2019, no. 16, pp. 1877–1881, Jan. 2019.

[17] X. Wang et al., "Structural reliability analysis of modular multilevel converters," *Proc. CSEE*, vol. 36, no. 7, pp. 1908–1914, 2016.

[18] L. Cheng et al., "Operational reliability analysis and application of MMC-based power electronic transformers," *Power Syst. Technol.*, vol. 46, no. 3, pp. 1073–1083, 2022.

[19] F. Yang et al., "Reliability evaluation model and application of multi-port cascaded power electronic transformers," *Power Syst. Protection Control*, vol. 47, no. 20, pp. 41–49, 2019.

[20] X. Shang, L. Pang, Q. Bu, and Q. Zhang, "Thermal runaway and induced electrical failure of epoxy resin in high-frequency transformers: Insulation design reference," *High Voltage*, vol. 9, no. 5, pp. 989–1000, Mar. 2024.

[21] R. Agarwal, H. Li, Z. Guo, and P. Cheetham, "The effects of PWM with high dv/dt on partial discharge and lifetime of medium-frequency transformer for medium-voltage (MV) solid state transformer applications," *IEEE Trans. Ind. Electron.*, vol. 70, no. 4, pp. 3857–3866, Apr. 2023.

[22] W. Wang, X. Wang, J. He, S. Li, and Y. Nie, "Electric stress and dielectric breakdown characteristics under high-frequency voltages with multi-harmonics in a solid-state transformer," *Int. J. Elect. Power Energy Syst.*, vol. 129, Jul. 2021, Art. no. 106861.

[23] D. Ma, W. Chen, L. Shu, X. Qu, and K. Hou, “A MMC-based multiport power electronic transformer with shared medium-frequency transformer,” *IEEE Trans. Circuits Syst. II, Exp. Briefs*, vol. 68, no. 2, pp. 727–731, Feb. 2021.

[24] H. Wang, G. Tang, Z. He, and J. Cao, “Power loss and junction temperature analysis in the modular multilevel converters for HVDC transmission systems,” *J. Power Electron.*, vol. 15, no. 3, pp. 685–694, May 2015.

[25] Y. Song, Y. Luo, and X. Xiong, “Loss distribution analysis and accurate calculation method for bulk-power MMC,” *Protection Control Modern Power Syst.*, vol. 8, no. 4, pp. 1–15, May 2023.

[26] H. Liu, K. Ma, Z. Qin, P. C. Loh, and F. Blaabjerg, “Lifetime estimation of MMC for offshore wind power HVDC application,” *IEEE J. Emerg. Sel. Topics Power Electron.*, vol. 4, no. 2, pp. 504–511, Jun. 2016.

[27] M. Handbook, “Reliability prediction of electronic equipment,” USA Dept. Defense, Tech. Rep. MILHDBK-217F, 1991.

[28] B. Abdi, A. H. Ranjbar, G. B. Gharehpetian, and J. Milimonfared, “Reliability considerations for parallel performance of semiconductor switches in high-power switching power supplies,” *IEEE Trans. Ind. Electron.*, vol. 56, no. 6, pp. 2133–2139, Jun. 2009.

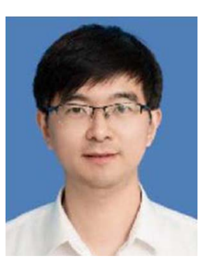

Jun Jiang (Senior Member, IEEE) was born in Anqing, China, in 1988. He received the B.E. degree in electrical engineering and automation from China Agricultural University, Beijing, China, in 2011, and the Ph.D. degree in high voltage and electrical insulation from North China Electric Power University, Beijing, China, in 2016.

From 2019 and 2020, he was with the High Voltage Engineering Division, Department of Electrical and Electronic Engineering, School of Engineering, The University of Manchester, Manchester, U.K., as Honorary Stuff/Academic Visitor. He is currently with the Department of Electrical Engineering, Nanjing University of Aeronautics and Astronautics, Nanjing, China. His research interests include condition monitoring of power apparatus and optical sensing application.

Beibei Chen was born in Zhoukou, China, in 2000. She received the B.E. degree in electrical engineering and automation from Soochow University, Suzhou, China, in 2023.

She is currently working toward the master’s degree in electrical engineering with the Nanjing University of Aeronautics and Astronautics, Nanjing, China. Her research interest incudes insulation reliability assessment of power electronic transformers.

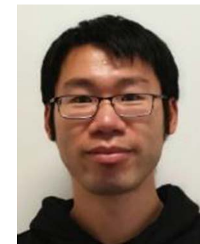

Qingwei Zhu received the Ph.D. in power electronics and power drive from the University of Chinese Academy of Sciences, Beijing, China, in 2016.

From 2016 to 2020, he was a Postdoctoral Researcher with the University of Manchester, Manchester, U.K. In 2021, he joined industry and had been an Associate Principal Power Electronics Engineer in CRRC Times Electric innovation Centre, Birmingham, U.K., contributing to the development of discrete power device-oriented, high power-density motor drive converters.

Xuefeng Duan was born in Xuzhou, Jiangsu, China, in 1983. He received the B.E. degree from the Yancheng Institute of Technology (YCIT), Yancheng, China, in 2005.

His research interests include powder processing and modification, collaborative control of atmospheric pollutants, comprehensive utilization of solid waste, and technical research on power semiconductor materials and packaging structures.

Renli Fu received the B.S. degree in physics from Yat-sen University, Guangzhou, China, in 1986, and the Ph.D. degree in mechanical design and theory from the China University of Mining and Technology, Beijing, China, in 1997.

He is currently a Full Professor with the College of Materials Science and Technology, Nanjing University of Aeronautics and Astronautics, Nanjing, China. His research focuses on high-performance composite materials for electronic packaging.